Measurement of transient deformations using digital image correlation method and high-speed photography: application to dynamic fracture

Madhu S. Kirugulige,[1] Hareesh V. Tippur,[1,*] and Thomas S. Denney[2]

[1]Department of Mechanical Engineering, Auburn University, Auburn, Alabama 36849, USA
[2]Department of Electrical and Computer Engineering, Auburn University, Auburn, Alabama 36849, USA

*Corresponding author: tippuhv@auburn.edu

Received 5 February 2007; accepted 13 April 2007;
posted 23 April 2007 (Doc. ID 79718); published 9 July 2007

The digital image correlation method is extended to the study of transient deformations such as the one associated with a rapid growth of cracks in materials. A newly introduced rotating mirror type, multichannel digital high-speed camera is used in the investigation. Details of calibrating the imaging system are first described, and the methodology to estimate and correct inherent misalignments in the optical channels are outlined. A series of benchmark experiments are used to determined the accuracy of the measured displacements. A 2%–6% pixel accuracy in displacement measurements is achieved. Subsequently, the method is used to study crack growth in edge cracked beams subjected to impact loading. Decorated speckle patterns in the crack tip vicinity at rates of 225,000 frames per second are registered. Two sets of images are recorded, one before the impact and another after the impact. Using the image correlation algorithms developed for this work, the entire crack tip deformation history, from the time of impact to complete fracture, is mapped. The crack opening displacements are then analyzed to obtain the history of failure characterization parameter, namely, the dynamic stress intensity factor. The measurements are independently verified successfully by a complementary numerical analysis of the problem.

OCIS codes: 100.2000, 120.6150, 120.0280, 350.4600, 070.4560, 120.3940.

1. Introduction

Measuring surface deformations and stresses in real time during a transient failure event, such as dynamic crack initiation and growth, in opaque materials is quite challenging due to a combination of spatial and temporal resolution demands involved. One of the earliest efforts in this regard dates back to the work of de Graaf [1]. In this work, a photoelastic measurement was attempted to witness stress waves around a dynamically growing crack in steel. This method continues to be popular in the study of fast fracture events [2,3]. In recent years, a lateral shearing interferometer called coherent gradient sensing (CGS) has become a tool of choice for studying dynamic fracture problems of opaque solids because of its robustness and insensitivity to rigid body motions [4–7]. Moiré interferometry has also been used in the past to measure in-plane displacement fields in dynamic fracture experiments [8]. The electronic speckle pattern interferometry (ESPI) and digital speckle photography [9–11] methods have been found suitable for measuring both in-plane as well as out-of-plane deformations in opaque solids. The former uses speckle intensity patterns formed by the illumination of an optically rough surface with coherent light. An interferogram containing a fringe pattern is formed when speckle images, recorded before and after deformation, are subtracted digitally or when a photographic film is exposed twice. In the latter, the intensity of the speckle images is compared digitally to determine the local translations of speckles. This method does not require any reference wave, and incoherent light is sufficient making it simple, robust, and easy to use. Using these methods, vibration measurements have been attempted by em-

0003-6935/07/225083-14$15.00/0

ploying a high-speed camera in Refs. 12, 13. Duffy's double aperture imaging scheme [14] has been modified by Sirohi *et al*. [15] to measure displacement derivatives using ESPI. Chao, *et al*. [16] studied deformations around a propagating crack using the digital image correlation method with the aid of a Cranz–Schardin film camera. In this work, they scanned film records obtained from the camera to perform correlation operations between successive images to estimate displacements. With the advent of new-generation digital high-speed cameras (with imaging rates from a few thousand to a few million frames per second), there has recently been a renewed interest in studying transient problems [17,18].

It should be noted here that photoelasticity and interferometric techniques can measure surface deformations in real time, but they require somewhat elaborate surface preparation (transferring of gratings in the case of moiré interferometry, preparing a specularly reflective surface in the case of CGS, preparing birefringent coatings in reflection photoelasticity, etc.). For cellular materials (syntactic foams, polymeric or metal foams, balsa wood, etc.) such surface preparations are rather challenging and, in some cases, may not be feasible at all. In those instances, the digital image correlation method with white light illumination is a very useful tool due to the relative simplicity in this regard. It involves decorating a surface with black and white paint mists alternatively. Recent advances in image processing methodologies and ubiquitous computational capabilities have made it possible to apply this technique to a variety of applications—in biomechanics to measure displacements of arterial tissues [19,20], in metal forming to measure deformations during cold rolling [21], and in carbon/carbon composites to measure displacements and strains [22], just to name a few. Early contributors to the development of this method include Peters and Ranson [23], and Sutton and his co-workers [24,25]. Chen and Chiang [26] subsequently developed a spectral domain approach to measure displacements of digitized speckle patterns. A stereo-vision methodology for measuring 3D displacement fields has also been introduced in recent times [27].

With the arrival of modern digital high-speed cameras, imaging rates as high as several millions frames per second can be achieved at a relatively high spatial resolution. This has opened the possibility of using digital image correlation (DIC) to estimate surface displacements and strains for extracting dynamic fracture/damage parameters. In the current work, the DIC technique is extended to mode-I dynamic fracture studies by estimating surface displacements near a stationary, as well as a propagating crack tip in edge cracked polymeric beams subjected to stress wave loading. A rotating mirror-type high-speed digital camera is used to record a spray-painted random speckle pattern in the crack tip vicinity. The entire crack tip deformation history from the time of impact to complete fracture is mapped. Since the current work uses a newly introduced multichannel digital high-speed imaging equipment, calibration of the recording system for DIC is undertaken. Tests are carried out to estimate misalignments between different optical channels of the camera and then correct them to get good optical registration. A series of benchmark experiments for the high-speed camera are conducted and the accuracy of the estimated displacements are reported.

2. Approach

In the digital image correlation technique, random speckle patterns on a specimen surface are monitored during a fracture event. These patterns, one before and one after deformation, are acquired, digitized, and stored. Then, a subimage within the undeformed image is chosen, and its location in the deformed image is sought. Once the location of a subimage in the deformed image is found, the local displacements can be readily quantified. In the current work, a three-step approach is developed in a MATLAB [28] environment to estimate two-dimensional (2D) displacements:

Step 1. Initial estimation of displacements. In the first step, a 2D cross correlation is performed between two selected subimages. The peak of the correlation function was detected to a subpixel accuracy of 1/16th of a pixel by bicubic interpolation. This process is repeated for the entire image to get full-field in-plane displacements. The process is briefly explained next.

Consider two subimages: $f(x, y)$ from the undeformed image and $g(x, y)$ from the deformed image (Fig. 1). Note that $g(x, y)$ can be approximated as a shifted copy of $f(x, y)$ with some random noise $\eta(x, y)$. That is, $g(x, y) = f(x - u, y - v) + \eta(x, y)$, where u and v denote displacements. The cross correlation can now be performed in the frequency domain as [26],

$$P(\omega_x, \omega_y) = \frac{F(\omega_x, \omega_y)G^*(\omega_x, \omega_y)}{|F(\omega_x, \omega_y)G^*(\omega_x, \omega_y)|^{1-\alpha}}, \qquad (1)$$

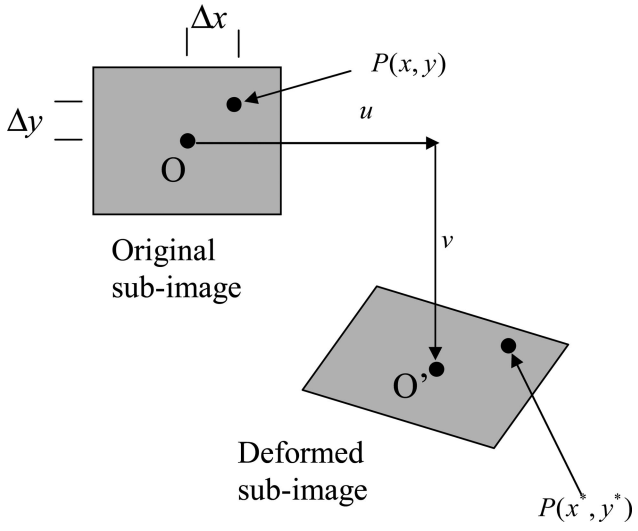

Fig. 1. Undeformed and deformed subimages chosen from images before and after deformation, respectively.

where F and G are Fourier transforms of $f(x, y)$ and $g(x, y)$ respectively, (ω_x, ω_y) are the frequency domain variables and α is a constant which can be varied from 0 to 1. By taking Fourier transform of the function $P(\omega_x, \omega_y)$, one can get a distinct peak in the second Fourier domain. Obtaining u and v displacements of a subimage then reduces to detecting the spatial location of the peak of the correlation function accurately. The quality of the signal peak (impulse function) depends on the chosen value of α. If $\alpha = 0$ is chosen, then in an ideal case (existence of zero noise in the images), the spectrum relation of Eq. (1) becomes a pure phase field and the response will degenerate into a Dirac delta function located at (u, v). But in reality, due to the presence of noise, the signal peak will be suppressed. Therefore, it is necessary to make $P(\omega_x, \omega_y)$ a halo-weighted complex spectrum rather than a pure phase field by choosing $\alpha > 0$. A systematic study about the selection of α and its effects on measured displacements can be found in [26]. In the current work, the constant $\alpha = 0.25$ is adopted. This ensured a good signal-to-noise ratio [the probability of a distinct peak appearing at (u, v) is maximized].

Step 2. Refining displacements. In this step, an iterative approach is used to minimize the 2D correlation coefficient by using a nonlinear optimization technique. The correlation coefficient is defined as [25]

$$s\left(u,\ v,\ \frac{\partial u}{\partial x},\ \frac{\partial u}{\partial y},\ \frac{\partial v}{\partial x},\ \frac{\partial v}{\partial y}\right) = 1 - \frac{\sum_{i,j}\left[F(x_i,\ y_j) - \bar{F}\right]\left[G(x_i^*,\ y_j^*) - \bar{G}\right]}{\sqrt{\sum_{i,j}\left[\left(F(x_i,\ y_j) - \bar{F}\right)^2\right]\sum_{i,j}\left[\left(G(x_i^*,\ y_j^*) - \bar{G}\right)^2\right]}}. \tag{2}$$

Here $F(x_i, y_i)$ is the pixel intensity or the gray scale value at a point (x_i, y_i) in the undeformed image and $G(x_i^*, y_i^*)$ is the gray scale value at a point (x_i^*, y_i^*) in the deformed image. The mean values of the intensity matrices F and G, respectively (Fig. 1), are denoted by $\bar{F}$ and $\bar{G}$. The coordinates or grid points (x_i, y_i) and (x_i^*, y_i^*) are related by the deformation that occurs between the two images. If the motion is in a plane perpendicular to the optical axis of the camera, then the relation between (x_i, y_i) and (x_i^*, y_i^*) can be approximated by a 2D affine transformation,

$$x^* = x + u + \frac{\partial u}{\partial x}\Delta x + \frac{\partial u}{\partial y}\Delta y,$$

$$y^* = y + v + \frac{\partial v}{\partial x}\Delta x + \frac{\partial v}{\partial y}\Delta y. \tag{3}$$

Here u and v are translations of the center of the subimage in the X and Y directions, respectively. The distances from the center of the subimage to a generic point (x, y) are denoted by Δx and Δy. Thus, the correlation coefficient, s, is a function of displacement components (u, v) and displacement gradients $(\partial u/\partial x, \partial u/\partial y, \partial v/\partial x$, and $\partial v/\partial y)$. Therefore, a search has to be performed for optimum values of displacements and their gradients such that s is minimized. In the current work, the Newton–Raphson method, which uses a line search and the Broyden, Fletcher, Goldfarb, and Shanno algorithm to update an inverse Hessian matrix, is employed [29]. This method is applied in two phases. In the first phase, minimization is done in only a two variable (u, v) space by using the initial estimates from Step 1. In the second phase, minimization is carried out in a six variable space (displacements and displacement gradients) by using values for (u, v) from Step 1 and zeros for all the gradients. It should be noted here that the estimation of displacements is accurate if the minimization is done in a six variable space rather than in a two variable space. However, the gradients obtained are quite noisy (this is especially true when gradients are small).

Step 3. Smoothing of displacements. The displacements obtained from the image correlation process represent average values for each subset and they tend to be noisy. Therefore it is necessary to apply smoothing algorithms to (u, v) fields. There are a number of methods available in the literature to smooth the data [30,31]. The one employed here uses an unbiased optimum smoothing parameter based on the noise level present in the displacement field. It should be noted here that displacements are discontinuous across the crack. Any generic smoothing method will smooth displacements across the crack faces and the strain concentration effects near the crack tip will be interpreted inaccurately. Therefore a smoothing method which allows a discontinuity of displacements across the crack faces was introduced. A regularized restoration filter [32] with a second order fit was employed for this purpose. This method minimizes the functional,

$$\phi(f) = \|g - \mathrm{H}f\|^2 + \alpha_s\|\mathrm{L}f\|^2, \tag{4}$$

where f is the restored displacement field and g is the noisy displacement field obtained from DIC, both arranged in a single column format. In Eq. (4), H is a point spread function (PSF) of a degradation model. The objective in the current work was to remove the random noise in order to restore/smooth displacement fields. Therefore, H was assumed to be an identity matrix. The Laplacian operator $(\partial^2/\partial x^2 + \partial^2/\partial y^2)$ is denoted by L in Eq. (4). Here α_s is a smoothing parameter selected on the basis of the noise present in the displacement filed. The operation $\|\cdot\|$ denotes l^2-norm of a vector. Now, Eq. (4) can be written as

$$\phi(f) = (g - \mathrm{H}f)^T(g - \mathrm{H}f) + \alpha_s f^T L^T \mathrm{L}f. \tag{5}$$

The above functional is minimized by differentiating $\phi(f)$ with respect to f and equating the result to zero. Upon simplification we get

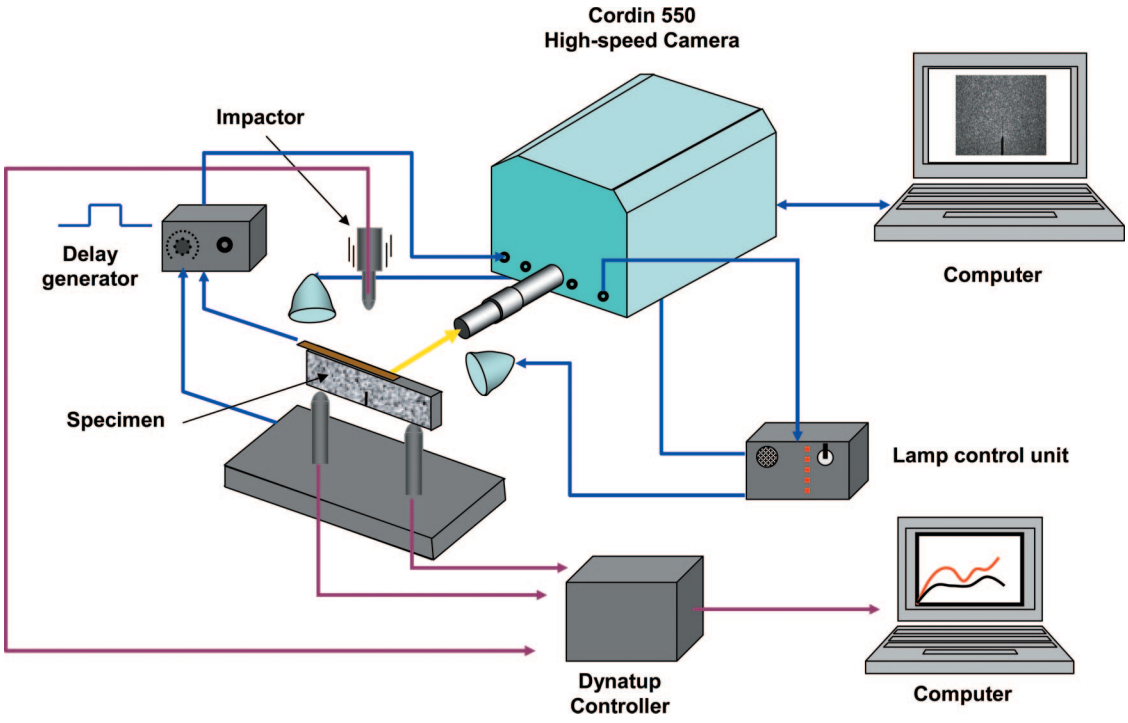

Fig. 2. (Color online) Schematic of the dynamic experimental setup.

$$f = (H^T H + \alpha_s L^T \mathrm{SL})^{-1} \mathrm{Hg}. \tag{6}$$

Here S is a diagonal matrix needed if a different amount of smoothing is desired in different parts of the image. In the current work, however, an identity matrix was used for S with appropriate diagonal elements set to zero to turn off smoothing across the crack. The Laplacian $(\partial^2/\partial x^2 + \partial^2/\partial y^2) = \nabla^2 f$ was found by defining a 3×3 Laplacian kernel [a 3×3 mask with four neighborhood points is most common even though other types of windows are used in the literature (a 3×3 mask with eight neighborhood points, a 5×5 mask, etc.)] as

$$L(m, n) = \begin{bmatrix} 0 & 1 & 0 \\ 1 & -4 & 1 \\ 0 & 1 & 0 \end{bmatrix}. \tag{7}$$

The data points corresponding to the crack faces were excluded from this operation so that displacement discontinuity was preserved along the crack faces. The smoothing parameter α_s was chosen so that data infidelity satisfies the condition [30,31]

$$\frac{1}{n} \sum_{j=1}^{n} [f(j) - g(j)]^2 = \sigma^2, \tag{8}$$

where n is the total number of data points. The quantity σ^2 is the variance of the noise present in the displacement data and will have to be estimated by a calibration process.

3. Dynamic Experimental Setup

A schematic of the experimental setup used in this study is shown in Fig. 2. It consisted of an Instron-Dynatup 9250-HV drop-tower for impacting the specimen and a Cordin 550 ultrahigh-speed digital camera (with a 28–300 mm macro lens) for capturing images in real time. The drop tower had an instrumented tup for recording the impact force history and a pair of anvils for recording support reaction histories. The setup also consisted of a delay/pulse generator to generate a trigger pulse when the tup contacts the specimen. Since all of the images were recorded during the dynamic event lasting over 100 μs, the setup used two high-energy flash lamps, triggered by the camera, to illuminate the specimen. The setup also utilized two computers, one to record the tup force and anvil reaction histories (5 MHz acquisition rate), and the other to record the images.

The high-speed camera uses a combination of CCD-based imaging technology and a high-speed rotating mirror optical system. It can capture images up to two million frames per second at a resolution of 1 K $\times$ 1 K pixels per image. It has 32 independent CCD image sensors positioned radially around a rotating mirror, which sweeps light over these sensors (Fig. 3). Each sensor is illuminated by a separate optical relay. Thus small misalignments between the images are to be expected. (The effect of these parameters on displacement results are discussed in Sections 4 and 5). *These misalignments preclude the possibility of performing image correlation between two images recorded by two different CCD sensors of the camera.* Hence, an alternative approach was adopted. Prior to impacting the specimen, a set of 32 images of the

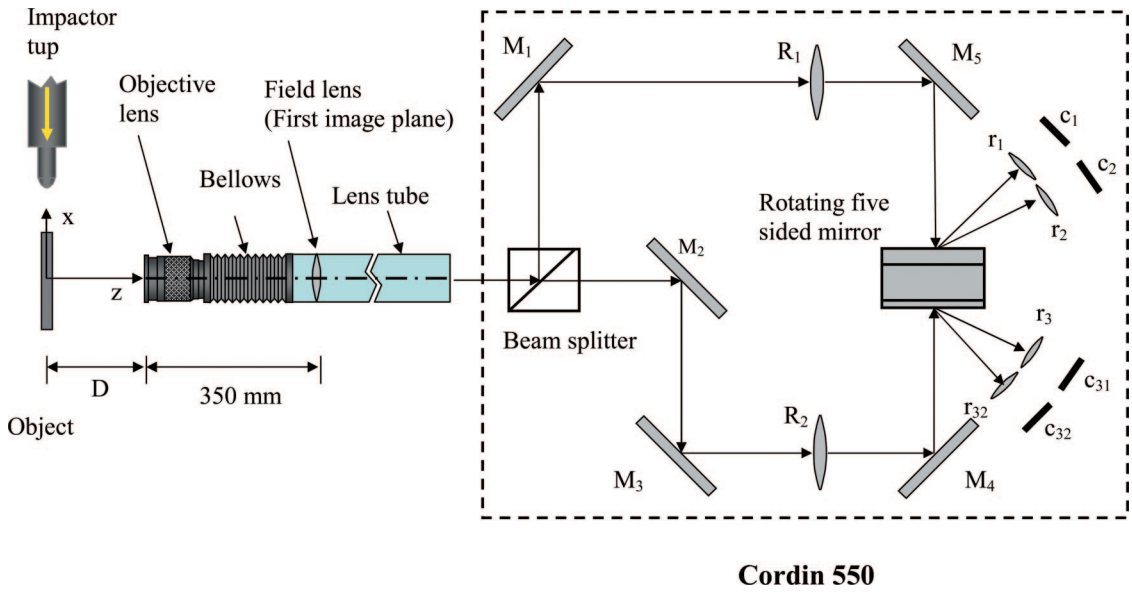

Fig. 3. (Color online) Optical schematic of cordin-550 camera: M1, M2, M3, M4, M5 are mirrors; R1 and R2 are relay lenses; r1, r2, . . . r32 are relay lenses for CCDs; c1, c2, . . . c32 are CCD sensors.

specimen was recorded at the desired framing rate (225,000 frames per second in this work). While keeping all the camera settings (CCD gain, flash lamp duration, framing rate, trigger delay, etc.) the same, a second set of images, this time triggered by the impact event, were captured. For *every image in the deformed set, there is a corresponding image in the undeformed set.* That is, if an image in the deformed set was recorded by sensor 10, then the image recorded by the same sensor (10) in the undeformed set was chosen for image correlation. To obtain meaningful results, it is essential that no extraneous camera movements occur while recording a set of images and during the time interval between the two sets of images. This was achieved by triggering the camera electronically in a vibration-free environment.

4. High-Speed Camera Calibration

As noted earlier, in the high-speed digital camera, different geometrical distortions are present in the images. This is because light travels through spatially different optical paths (relays) before reaching the individual CCD sensors (shown in Fig. 3). In this work, the specimen was located approximately 270 mm away from the objective lens. The field lens was approximately 620 mm away from the specimen. The image at the field lens was then relayed through various optical elements before being recorded by a sensor. For the camera system, four main types of misalignments in the images can be identified.

(1) *Focusing errors between optical relays:* This aberration can be minimized by careful alignment of each optical path, but cannot be entirely eliminated. However, since two images recorded from the same camera, one before and one after deformation, were correlated in the current work, this error does not affect the measurements.

(2) *Translation between two successive images:* The images could have an in-plane (X and Y directions) relative translation of 5–7 pixels (out of a 1000×1000 pixel image). Since the evaluation of the fracture parameters depends primarily on locating the crack tip, translation of the whole image is not detrimental to the accuracy of results. However, these translations between frames were estimated accurately by performing calibration. Subsequently, the images were aligned to get a good registration of one frame relative to the next.

(3) *In-plane rotation between two successive images:* The individual camera images could also have a relative rotation (a maximum of 0.003 radians between the frames) between them. This rotation was estimated accurately in the calibration experiment, and then the frames were aligned with respect to a chosen reference frame.

(4) *Perspective effect:* In order to minimize errors due to perspective effects, the camera needs to be located sufficiently far away from the specimen, and the images must be recorded using higher lens F numbers. In the current experiment, the field lens was situated ~620 mm away from the specimen.

A calibration experiment was performed to quantify the above misalignments. The objective here was to estimate the correction parameters to be used for aligning each optical channel relative to a reference. A template with 5×5 arrays of targets (black circles) was printed (on a white glossy background) and affixed to a flat surface (other investigators have used different array sizes ranging from 4×4 to 10×10, depending upon their application). The camera was focused on the template and the flash lamps were adjusted to illuminate the targets uniformly. A set of 32 pictures of the template was recorded at the de-

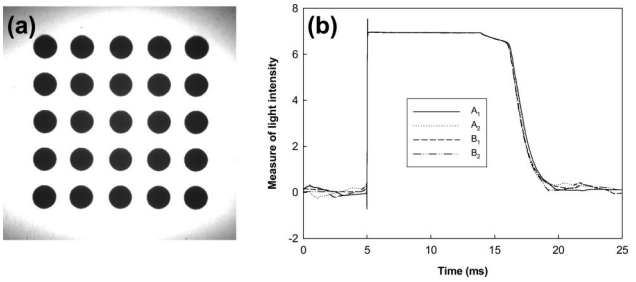

Fig. 4. (a) Image of the 5 × 5 dot pattern template used for calibration experiment, (b) photo detector output proportional to flash lamp light intensity, where A_1, A_2 and B_1, B_2 are two repeated acquisitions when the photodiode was placed 1 in. away in the plane perpendicular to optical axis of the camera.

sired rate (225,000 frames per second). Figure 4(a) shows a corresponding image recorded by one of the sensors. It should be noted here that calibration of the camera is needed only once before the actual experiments at the same framing rate. The various recording parameters (distance between the lens and the specimen, framing rate, magnification, etc.) subsequently need to be maintained nearly the same between the calibration and the actual experiments.

In the calibration experiment, correction of distortions was carried out using a two-step process. In the first step, various correction factors were estimated among the images. To do this, one image was chosen as the base image and the distortions of all of the other 31 images (called input images) with respect to the base image were estimated. The basè image and one of the input images were considered, and histogram equalization was carried out on them. Then these images were converted into binary images by performing a thresholding operation followed by an intensity inversion operation to get white circles with a black background. The location of the center of each circle was estimated for both the base and the input image. These center locations (also called control points) were further fine tuned for the input image by performing a normalized cross-correlation operation locally. This process is repeated for all other 31 images and the control points for every base image-input image pair were stored.

In the second step, correction was applied to the real images recorded in an experiment based on the transform inferred from the control points. (Here it should be emphasized that no histogram equalization and thresholding operations were performed on real images). The input image was transformed with respect to the base image by a linear conformal mapping transformation. In this transformation, the shape of the input image was unchanged, but the image was deformed by some combination of translation and rotation. While doing this, straight lines remained straight, and parallel lines remained parallel. The transformation used is given by

$$\begin{pmatrix} x_i \\ y_i \end{pmatrix} = \begin{pmatrix} a_1 & b_1 \\ -b_1 & a_1 \end{pmatrix} \begin{pmatrix} x_b \\ y_b \end{pmatrix} + \begin{pmatrix} a_0 \\ b_0 \end{pmatrix}, \tag{9}$$

Table 1. Alignment Differences Between Individual Optical Channels of a Cordin 550 Camera; Stretch, Rotation and Translations of Different Images with Respect to the Image Taken by Camera Number 09

	A_1	b_1 (radians)	a_0 (pixels)	b_0 (pixels)
Camera 00	0.9966	0.0003	1.3468	1.9695
Camera 01	0.9997	0.0004	−0.4052	−1.0066
Camera 02	0.9986	0.0003	0.7136	0.8484
Camera 03	1.0006	0.0002	−1.7187	0.0524
Camera 04	0.9986	−0.0009	0.5622	−0.1669
Camera 05	1.0001	−0.0003	−1.1137	−0.3886
Camera 06	1.0002	0.0007	−2.2279	−0.3266
Camera 07	1.004	0.0029	−6.5381	2.656
Camera 08	1.007	0.0056	−3.7658	−1.05
Camera 09	**1.0000**	**0.0000**	**0.0000**	**0.0000**
Camera 10	0.9983	−0.0019	0.0058	−0.9471
Camera 11	0.9995	−0.0012	1.6056	−1.9433
Camera 12	0.9946	−0.0003	8.1177	−0.6218
Camera 13	1.0003	0.0002	0.318	−0.2026
Camera 14	0.998	−0.0015	2.2551	−0.7557
Camera 15	0.9961	0.0005	2.6524	3.1431
Camera 16	0.9939	−0.0017	9.4083	1.9072
Camera 17	0.9977	−0.0005	4.6258	−0.7484
Camera 18	0.9984	−0.0003	5.4465	−1.8866
Camera 19	0.9969	−0.0013	4.5083	−1.7703
Camera 20	0.999	−0.0008	3.8725	−1.873
Camera 21	1	−0.0009	3.2238	−3.2697
Camera 22	0.9993	−0.0011	4.8201	−2.9866
Camera 23	1.0018	−0.0008	3.2343	−3.8285
Camera 24	0.9998	0.0006	3.7571	−1.9882
Camera 25	1.0017	−0.0012	1.4998	−4.764
Camera 26	0.999	0.0001	1.7903	−1.4227
Camera 27	0.9976	−0.0012	4.97	−0.3825
Camera 28	0.9999	−0.0007	4.1851	−2.8842
Camera 29	0.9984	−0.0014	4.5328	−2.8868
Camera 30	1.0002	−0.0019	4.1973	−3.5948
Camera 31	0.9995	−0.0016	3.2673	−2.8311

where (x_i, y_i) and (x_b, y_b) are coordinates of the input image and the base image, respectively. Also, (a_o, b_o) represent translations in the X and Y directions, respectively. The stretch and rotation are denoted by a_1 and b_1. Since there are four unknowns in Eq. (9), two pairs of control points are sufficient to find these unknowns. Since there are 25 pairs of control points (5 × 5 array), the unknowns were determined in this work in an overdeterministic least-squares sense. The transformation structure generated from each pair of control points is listed in Table 1. Here the image from camera 09 was chosen as the base image, and the misalignment of all other images with respect to this image is listed. It can be noted from this table that there is a horizontal and vertical misalignment between the images. The horizontal movement is in the range from 0 to 9 pixels, where the vertical movement is in the range of 0 to 4 pixels. Rotation between the frames is within 0.005 radians.

As noted earlier , for every experiment, two sets of images were recorded: one set before impact loading and one set after. The above transformations were applied for both sets. If a control points pair came

from analyzing images of sensors 1 and 10 (1 being the base image and 10 being the input image) of the reference image set, then the transformation was also applied to the images captured by sensors 1 and 10 in the undeformed set as well as the deformed set. The image correlation was then performed between the two images from the same camera (That is, between the images captured by sensor 10 of the undeformed set and the deformed set). Again it should be noted here that since the same transformations are applied to both the undeformed and deformed images, they would not influence measured deformations but improve the quality of sequential displaying or animation of images, which is helpful in the visualization of the failure process.

One of the main assumptions while performing image correlation between the two images recorded by a high-speed digital camera system is that illumination of the specimen is uniform and stable (spatially as well as temporally) and also repeatable. Spatial stability means that the light intensity needs to be uniform in the region of interest (in the current work 31×31 mm^2 area). For temporal stability, the light intensity is expected to remain constant during the event of interest (145 μs in this work during which all 32 images were acquired). The repeatability is also important since the light intensity needs to remain the same between two successive experiments. To be more specific, the undeformed set of 32 images and the deformed set of 32 images must be exposed by the same intensity of light.

The light intensity from the flash lamps initially ramps up, dwells for a while, and then decreases. The dwell time can be specified prior to an experiment. In the current work, the dwell time was set to 9 ms. In order to test flash lamp characteristics, a photodetector with a 1 mm^2 sensing area was placed at a location where the sample was placed in a fracture experiment. The voltage signal proportional to the light intensity was recorded with time using a high-speed data acquisition system at a sampling rate of 1 MHz. This exercise was repeated twice in order to check for the repeatability of the flash lamp characteristics. Now the photodetector is moved to a new location in the plane perpendicular to the optical axis of the camera by 1 in., and the output was recorded again twice. The voltage signal given by the photodetector is plotted in Fig. 4(b). Excellent repeatability in the light intensity can be seen from this figure. A dwell time of 9 ms can be seen from all of these plots. While conducting the fracture experiment, all of the images were recorded during this dwell time by appropriately triggering the event in the camera system. Thus, the flash lamps were found to be stable and no hot spots were found in the captured images.

5. Benchmark Experiments

Before discussing displacements and the associated results from the dynamic fracture tests, a few results from benchmark experiments are presented. In these experiments, a specimen (decorated with random black and white speckle pattern) was mounted on a 3D-translation stage (shown in Fig. 5). A series of known displacements were imposed in the X and Y directions separately and the images were captured. The mean and standard deviations of the obtained displacement fields were computed and compared with the applied displacements. Also, a small out-of-plane (Z direction) displacement of 30 ± 2 μm was applied to the sample and a set of images were captured. (This is typically the amount of out-of-plane displacement that occurs in the vicinity of a crack tip in an experiment conducted in this work. For example, in Ref. 7 one can see roughly seven to nine fringes near the crack tip over a distance of ~10 mm. Since these fringes represent surface slopes and the resolution of the CGS setup is ~0.015°/fringe, one can estimate the out-of-plane displacement around the crack tip to be ~23 μm.) The objectives of these benchmark experiments are as follows:

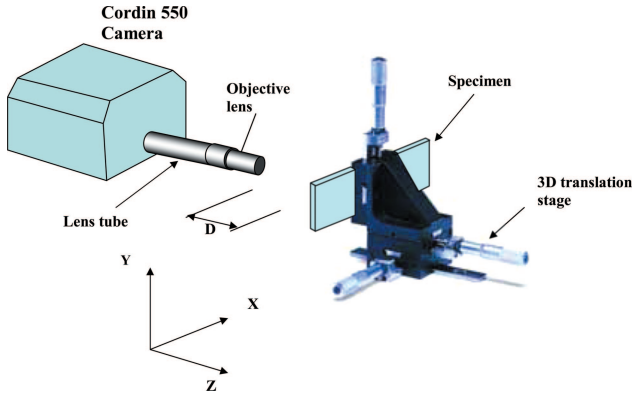

Fig. 5. (Color online) Experimental setup for conducting benchmark experiments for the high-speed digital camera.

- To estimate noise levels in the measured in-plane displacement fields (or, to determine the smallest in-plane displacement that can be measured reliably from the camera system).
- To compare displacement fields obtained by the 32 individual cameras when they are used to measure the same applied displacement.
- To determine the effect of out-of-plane displacement on the accuracy of measured in-plane displacements (or, to address the issue of whether the accuracy of in-plane displacements is affected if the sample undergoes small out-of-plane deformation during an experiment).
- To determine the effect of working distance D [distance between the sample and the objective lens (see Fig. 5)] on the quality of measured in-plane displacements.

The details of the benchmark experiments are given in Table 2. In total, six sets of 32 images were recorded in each configuration. In configuration 1, the objective lens of the camera system was 400 mm away from the sample. The first set of 32 images of the undeformed sample makes set 1. In set 2 and set

Table 2. Details of Benchmark Experiments: Six Sets of 32 Images Were Recorded in Each Configuration. In Configuration 2, the Camera was Kept Twice as Close as in Configuration 1

Configuration 1	Configuration 2
Working distance (D) = 400 ± 1 mm	Working distance (D) = 200 ± 1 mm
Magnification = 35.6 μm/pixel	Magnification = 27 μm/pixel
set 1 Undeformed	set 1 Undeformed
set 2 X translation = 60 ± 2 μm	set 2 X translation = 60 ± 2 μm
set 3 Y translation = 60 ± 2 μm	set 3 Y translation = 60 ± 2 μm
set 4 X translation = 300 ± 2 μm	set 4 X translation = 300 ± 2 μm
set 5 Y translation = 300 ± 2 μm	set 5 Y translation = 300 ± 2 μm
set 6 Z translation = 30 ± 2 μm	set 6 Z translation = 30 ± 2 μm

3, images were recorded after applying a 60 ± 2 μm translation in the X direction and a 60 ± 2 μm translation in the Y direction, respectively. This is typically the deformation level observed in the current tests. In set 4 and set 5, the specimen was translated by 300 ± 2 μm in the X direction, and 300 ± 2 μm the Y direction, respectively. These represent the amount of rigid body displacements expected in the dynamic tests. In set 6, images were recorded after applying a 30 μm translation in the Z direction. The same exercise was repeated for configuration 2, where the camera was kept twice as close as in configuration 1.

Full-field displacements were computed for all these tests. The subimage size chosen was 30 × 30 pixels which gave 32 × 32 = 1024 data points for a 1 × 1 K image pair. The results shown in Figs. 6(a) and 6(b) are: (i) mean and standard deviations of u displacement (between images of set 1 and set 2 of configuration 1, solid circles); (ii) mean and standard deviations of v-displacement (between images of set 2 and set 3 of configuration 1, solid squares); (iii) mean and standard deviations of u displacement (between images of set 1 and set 2 of configuration 2, solid triangles); and (iv) mean and standard deviations of v displacement (between images of set 1 and set 2 of configuration 2, solid diamonds). Tests were conducted in configuration 2 to examine the effect of working distance D on the accuracy of the displacements. It should be noted that magnification in con-

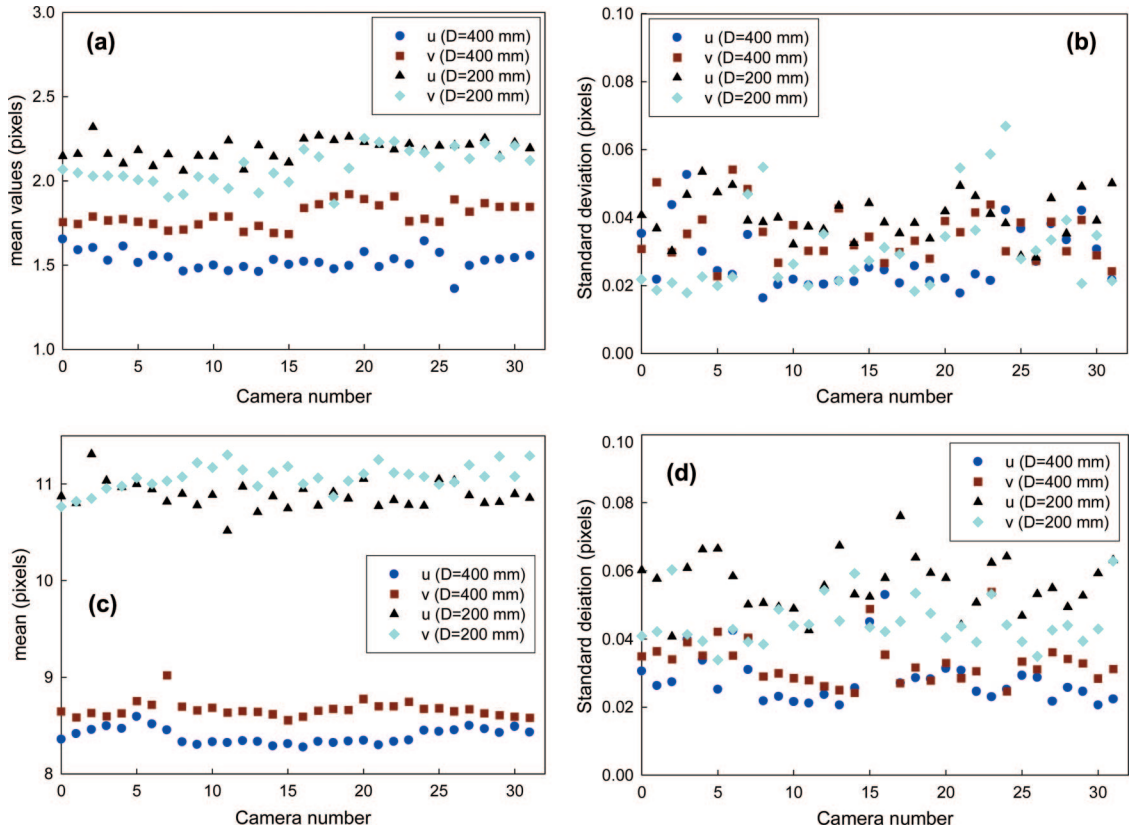

Fig. 6. (Color online) Benchmark experiment results for D = 400 mm and 200 mm (see Fig. 5): (a) mean and (b) standard deviations of u and v-displacement fields for X and Y translations of ~60 μm; (c) mean and (d) standard deviations of u- and v-displacement fields for X and Y translations of 300 μm. Magnification = 35.6 μm/pixel for D = 400 mm and 27 μm/pixel for D = 200 mm.

figuration 1 is 35.6 μm/pixel and in configuration 2 is 27 μm/pixel on the image plane. In view of this, a constant value of ~60 μm (1.6 pixels) was expected for the solid circles and solid squares of Fig. 6(a). Similarly a value of ~2.2 pixels was expected for the solid triangles and solid diamonds of Fig. 6(a). It can be seen from Fig. 6(a), that a constant displacement is being measured in all 32 cameras within a scatter band of 0.2 pixels. Also the error levels in the displacements measured by each of the cameras lie in the range of 2% to 6% of a pixel, can be seen in Fig. 6(b). Similar results for X and Y translations of 300 μm (between images of sets 1 and 4 and sets 1 and 5 of configurations 1 and 2) are presented in Figs. 6(c) and 6(d). By comparing the results of Figs. 6(b) and 6(d), it is evident that there is no significant difference in the standard deviations of measured displacement fields. This implies that displacements of 8–10 pixels can be measured rather easily to an accuracy of less than 6% of a pixel. By comparing the values of the solid triangles and solid circles in Fig. 6(b) or 6(d), it is clear that the quality of measured displacements is not affected significantly if the working distance D is reduced by a factor of 2. Finally, Fig. 7 shows the effect of the imposed out-of-plane displacement on the in-plane displacements measured. The mean and standard deviation of the u and v displacements that occurred between the images of sets 5 and 6 (Z translation of 30 μm) are given in Figs. 7(a) and 7(b). Again, both u and v displacements are within 0.1 pixels in Fig. 7(a). The standard deviation of u and v displacements is in the range of 1% to 6% of a pixel as is evident from Fig. 7(b).

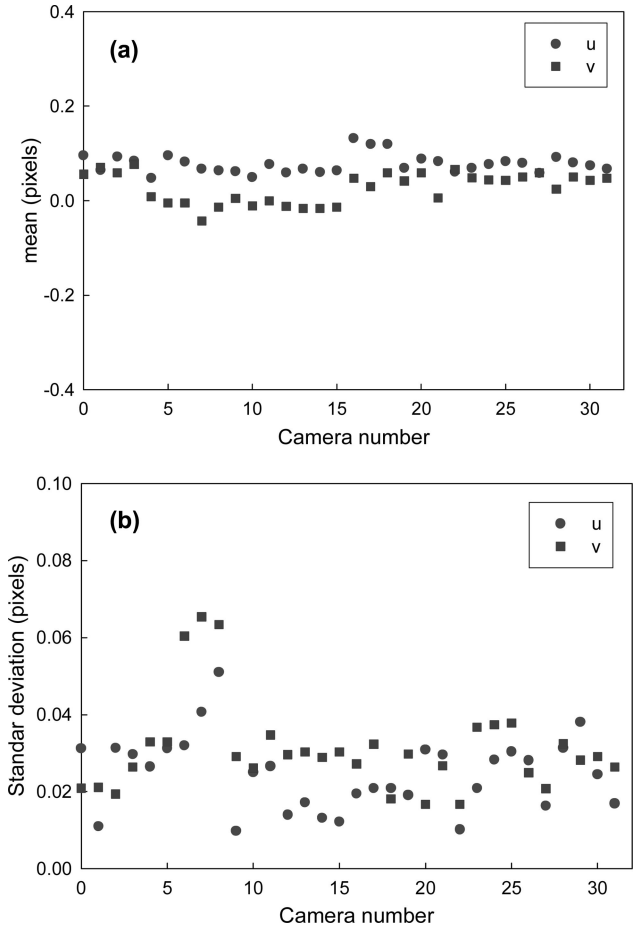

Fig. 7. Benchmark experiment results for D = 400 mm (see Fig. 5) and out-of-plane displacement (w) = 30 μm: (a) mean and (b) standard deviation of u and v-displacement field.

6. Dynamic Fracture Experiment

A. Sample Preparation

Edge cracked samples were prepared for conducting mode-I dynamic fracture experiments. These samples were made from epoxy (prepared by mixing a bisphenol-A resin and an amine based hardener in the ratio 100:38). The elastic modulus and Poisson's ratio of the cured material measured ultrasonically were 4.1 GPa and 0.34 respectively [33]. Before casting the epoxy resin-hardener mixture, a sharp razor blade was inserted into the mold. When the sample was cured and removed from the mold, a sharp-edged "notch" was left behind in the specimen. Further details about this method can be found in Ref. 34. Finally, the specimen was machined into a beam in 50 mm height with a crack of 10 mm in length (a/W = 0.2) [shown in Fig. 8(a)]. A random speckle pattern was created on the specimen surface by spray painting with black and white paint mists alternatively.

B. Experimental Procedure

Since the event to be captured is highly transient in nature, the total recording time is rather small and hence the high-speed camera was synchronized with the event. The sequence of events in a typical experiment was as follows

(1) The specimen was initially rested on two instrumented supports/anvils. The camera, anchored firmly to the ground, was focused on a 31 × 31 mm^2 region of the sample in the crack tip vicinity [see Fig. 8(a)].

(2) A set of 32 pictures of the stationary sample were recorded at 225,000 frames per second and stored.

(3) Next, an impactor was launched at a velocity of 4.5 m/s toward the sample. As soon as the tup made contact with an adhesive backed copper tape, affixed to the top of the specimen, a trigger signal was generated by a pulse/delay generator and was fed into the camera.

(4) The camera sent a separate trigger signal to two symmetrically placed high intensity flash lamps. A trigger delay was preset in the camera system to capture images 70 μs after the initial impact. This time delay provides sufficient time for the high intensity flash lamps to ramp up to their full intensity levels and provide uniform illumination during recording. Since measurable deformations around the crack tip for the first 70 μs are relatively small, there was no significant loss of information during this period. A total of 32 images were recorded with a

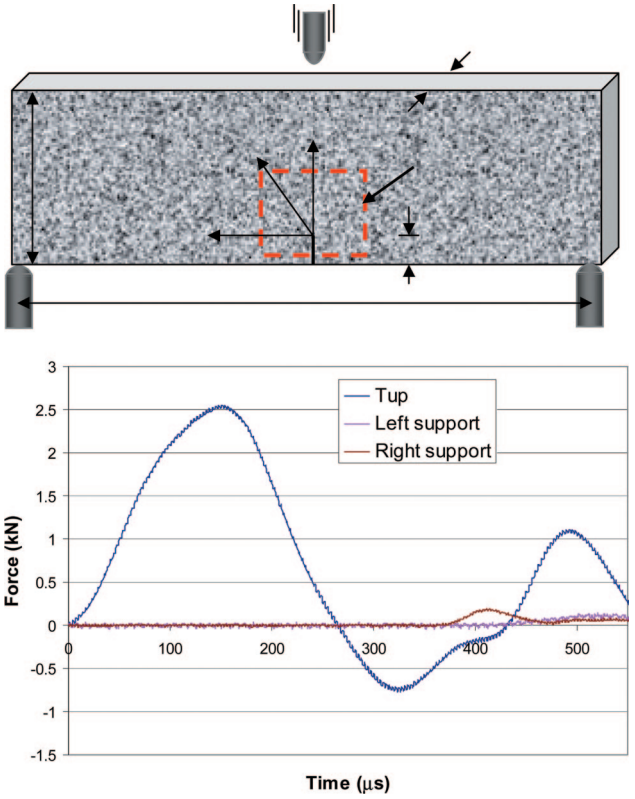

Fig. 8. (Color online) (a) Specimen configuration for mode I dynamic fracture experiment and (b) impactor force history and support reaction histories recorded by Instron Dynatup 9250 HV drop tower.

4.44 μs interval between images for a total duration of 160 μs.

(5) Once the experiment was completed, the recorded images were stored in the computer. Just before the impact occurs, the velocity of the tup was recorded by the Dynatup drop-tower system. Also recorded were histories of tup force and support reactions, shown in Fig. 8(b). In this plot, the tup making multiple contacts with the specimen as shown by more than one peak can be seen. The crack initiation in this experiment occurred at about 133 μs and the specimen failed at about 240 μs. Therefore only the first peak of the impact force history is of relevance here. The impact force was recorded by both left and right anvils. Also, it should be noted that anvils register a noticeable impact force after 380 μs by which time the crack propagates through one-half of the sample width. Therefore the reactions from the anvils do not play any role in the fracture of the sample up to this point. Accordingly, the sample was subsequently modeled as a free-free beam in numerical simulations with specimen inertia resisting the impact forces.

C. Numerical Simulations

Elastodynamic finite element simulations of the current problem were conducted up to crack initiation under plane stress conditions. Experimentally determined material properties (elastic modulus = 4.1 GPa, Poisson's ratio 0.34, and mass density = 1175 kg/m^3) were used as inputs for finite element analysis. The symmetric finite element model was loaded using one-half of the force history recorded by the instrumented tup. (Before applying, the force history data were interpolated and smoothed for two reasons: (a) the time step of the force history measurement was larger than the one used in the simulations, and (b) the force history recorded by the tup had experimental noise. Therefore smoothed cubic splines were fitted to the force history data before applying them to the model.) The implicit time integration scheme of the Newmark β method with parameters $\beta = 0.25$ and $\gamma = 0.05$, and 0.5% damping was adopted in the simulations. The details of finite element analysis are avoided here and can be found elsewhere [34]. The simulation results were used to obtain instantaneous stress intensity factors up to crack initiation. The stress intensity factor was calculated by a regression analysis of crack opening displacements and the T stress was determined using a modified stress difference method [34].

D. Surface Deformation History

From each experiment 64 images were available, 32 from the undeformed set and 32 from the deformed set, each having a resolution of 1000 × 1000 pixels. Figure 9 shows four selected speckle pattern images from the deformed set of 32 images. The time instant at which the images were recorded after impact is indicated below each image and the current crack tip is denoted by an arrow. The position of the crack tip is plotted against time in Fig. 10. It can be seen from this figure that the crack initiates at about 175 μs. Upon initiation, the crack rapidly accelerates and

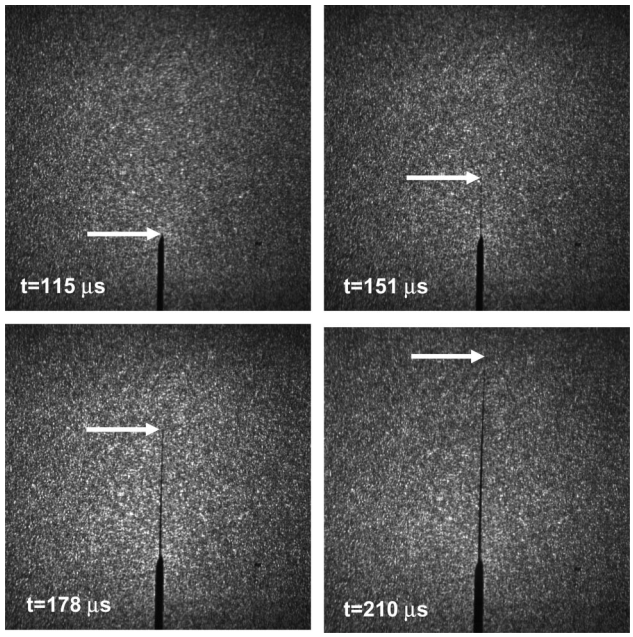

Fig. 9. Acquired speckle images of 31 × 31 mm^2 region at various times instances; current crack tip location is shown by an arrow.

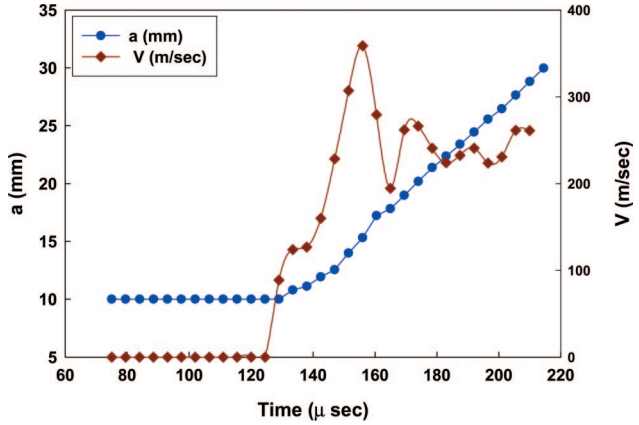

Fig. 10. (Color online) Crack growth behavior in epoxy sample under mode-I dynamic loading; crack length history and crack speed history.

subsequently propagates at a relatively steady velocity of ~270 m/s. The magnification used in this experiment was such that the size of a pixel was equal to 31 μm on the specimen. A subimage size of 26 × 26 pixels was chosen for image correlation. The in-plane displacements were estimated for all the 32 image pairs. The crack opening displacement, v, and sliding displacement, u, for two sample images (one before crack initiation and one after) are shown in Fig. 11. Figures 11(a) and 11(c) show v and u displacements at 150 μs after impact and Figs. 11(b) and 11(d) show the corresponding displacement components at t = 220 μs after impact. All of these are smoothed values of displacements. A significant amount of rigid body displacement component can be seen in the u field [Figs. 11(c) and 11(d)]. In the current work, the displacements were resolved to an accuracy of 2% to 6% of a pixel, or 0.6 to 1.8 μm.

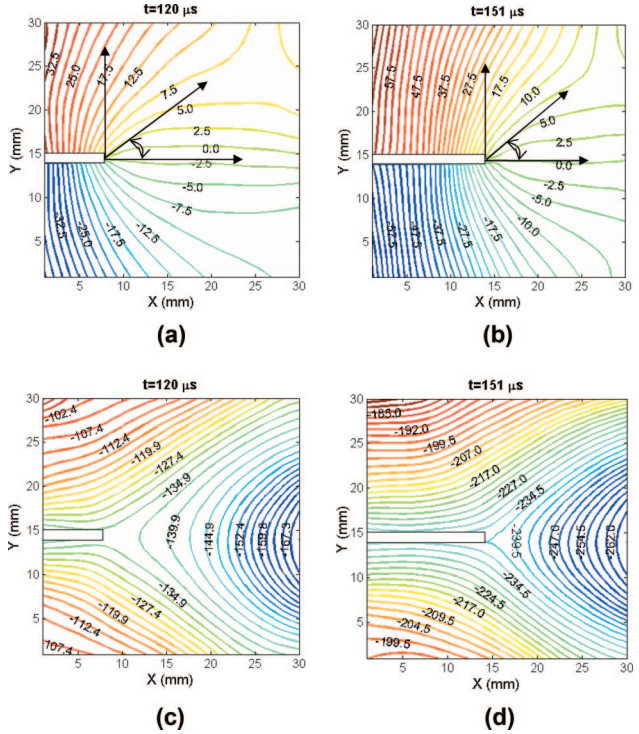

Fig. 11. (Color online) Crack opening and sliding displacements (in μm) for pre-crack and post-crack initiation instants: (a) v displacement and (c) u displacement before crack initiation (at t = 120 μs); (b) v displacement and (d) u displacement after crack initiation (t = 151 μs); crack initiation time ~133 μs.

E. Extraction of Stress Intensity Factors from Measured Displacements

The crack opening displacement (v) field (displacement in the Y direction) was used to extract dynamic stress intensity factors in the current work. The asymptotic expression for this field for a dynamically loaded stationary crack is given by [35]

$$v = A_0(t)\frac{r^{1/2}}{\mu}\sin(\theta/2)\left(\frac{2}{1+\nu} - \cos^2(\theta/2)\right) - \frac{\nu B_0(t)}{\mu(1+\nu)} \times r\sin\theta - C_0(t)\frac{r^{1/2}}{\mu}\cos(\theta/2)\left(\frac{1-\nu}{1+\nu} - \sin^2(\theta/2)\right) - \frac{D_0(t)}{\mu(1+\nu)} r\cos\theta + \mathrm{Pr}\cos\theta + \mathrm{Qr}\sin\theta + \mathrm{Cr}^0 + O(r^{3/2}). \quad (5)$$

In the above equation, (r, θ) are crack tip polar coordinates and μ, ν are shear modulus and Poisson's ratio of the material. Also, A_0, B_0, C_0, D_0, P, Q, and C are constant coefficients of the asymptotic expansion. Mode I and mode II dynamic stress intensity factors $K_I(t)$ and $K_{II}(t)$ are related, respectively, to the constants A_0 and C_0 as $K_I(t) = A_0\sqrt{2\pi}$ and $K_{II}(t) = C_0\sqrt{2\pi}$. The quantity $2B_0(t)$ is the so-called T stress. In Eq. (5), the first two terms represent symmetric deformations (mode I), the third and fourth terms represent antisymmetric deformation (mode II), the fifth, sixth, and seventh terms are to account for rotation and rigid body translations. Equation (5) implicitly assumes that inertial effects enter the coefficients while retaining the functional form of the quasistatic crack tip equation.

Once the crack initiates, a different set of equations need to be used. Asymptotic expression for crack opening displacement field for a steadily propagating crack is given by [36]

$$v = \sum_{n=1}^{\infty}\frac{(K_I)_n B_I(C)}{2\mu}\sqrt{\frac{2}{\pi}}(n+1)\left\{-\beta_1 r_1^{n/2}\sin\frac{n}{2}\theta_1 + \frac{h(n)}{\beta_2} r_2^{n/2}\sin\frac{n}{2}\theta_2\right\} + \sum_{n=1}^{\infty}\frac{(K_{II})_n B_{II}(C)}{2\mu}\sqrt{\frac{2}{\pi}} \times (n+1)\left\{\beta_1 r_1^{n/2}\cos\frac{n}{2}\theta_1 + \frac{h(\bar{n})}{\beta_2} r_2^{n/2}\cos\frac{n}{2}\theta_2\right\} + \mathrm{Pr}\cos\theta + \mathrm{Qr}\sin\theta + \mathrm{Cr}^0, \quad (6)$$

where

$$r_m = \sqrt{X^2 + \beta_m{}^2 Y^2}, \qquad \theta_m = \tan^{-1}\left(\frac{\beta_m Y}{X}\right), \quad m = 1,\ 2,$$

$$\beta_1 = \sqrt{1 - \left(\frac{c}{C_L}\right)^2}, \qquad \beta_2 = \sqrt{1 - \left(\frac{c}{C_s}\right)^2},$$

$$C_L = \sqrt{\frac{(\kappa + 1)\mu}{(\kappa - 1)\rho}}, \qquad C_S = \sqrt{\frac{\mu}{\rho}},$$

$$\kappa = \frac{3 - \nu}{1 + \nu} \text{ for plane stress},$$

$$h(n) = \begin{cases} \dfrac{2\beta_1\beta_2}{1 + \beta_2{}^2} & \text{for odd } n \\ \dfrac{1 + \beta_2{}^2}{2} & \text{for even } n \end{cases} \quad \text{and } h(\bar{n}) = h(n + 1),$$

$$B_{\mathrm{I}}(c) = \frac{(1 + \beta_2{}^2)}{D}, \qquad B_{\mathrm{II}}(c) = \frac{2\beta_2}{D},$$

$$D = 4\beta_1\beta_2 - (1 + \beta_2{}^2)^2. \tag{7}$$

Here (X, Y) and (r, θ) are crack tip Cartesian and polar coordinates instantaneously aligned with the current crack tip [see Fig. 11(b)]. Note that c is the speed of the propagating crack tip, C_L and C_S are dilatational and shear wave speeds in the material, μ and ν are shear modulus and Poisson's ratio, respectively. The coefficients $(K_{\mathrm{I}})_n$, and $(K_{\mathrm{II}})_n$ of the singular terms are the mode I and mode II dynamic stress intensity factors, respectively. The coefficient of the second term of the mode I series is related to the remote stress component $\sigma_{ox}{}^{dyn}$ $[= 3(K_{\mathrm{I}})_2(\sqrt{2/\pi})]$. The quantity $\sigma_{ox}{}^{dyn}$ is a parameter that controls crack curving and branching.

For extracting the stress intensity factor from the displacement data, the current crack tip location was identified and the Cartesian and polar coordinate systems ($X - Y$ and $r - \theta$) were established at the crack tip. A number of data points were collected [usually 100–120) in the region around the crack tip ($0.3 < r/B < 1.6$) and $-135° < \theta < 135°$, where B is the sample thickness], and the displacement values as well the location of these points were stored. An over deterministic least-squares analysis [37] of the data was carried out in order to find K_{I}, K_{II}, and B_o. This was repeated for all 32 image pairs, and the stress intensity factor history was generated. The crack opening displacement field obtained from the DIC, superposed with the ones obtained from the least-squares fit of the stress intensity factor solution, is shown for two time instants (one before crack initiation and one after) in Fig. 12. The synthetic contours are plots of Eq. (5) in Fig. 12(a) and Eq. (6) in Fig. 12(b) with only K-dominant terms. The least-squares fit considering the K dominant solution shows a good agreement with the experimental data.

Figure 13(a) shows the stress intensity factor history extracted from displacements. The crack initiation time is indicated by a vertical dotted line. The mode I stress intensity factor, K_{I}, increases monotonically up to crack initiation at 133 μs. Following initiation at $K_{\mathrm{I}} = 1.1$ MPa $\mathrm{m}^{1/2}$ the stress intensity factor continues to increase until it reaches a value of ~1.7 MPa $\mathrm{m}^{1/2}$, beyond which it appears to remain constant until ~200 μs, and beyond which images

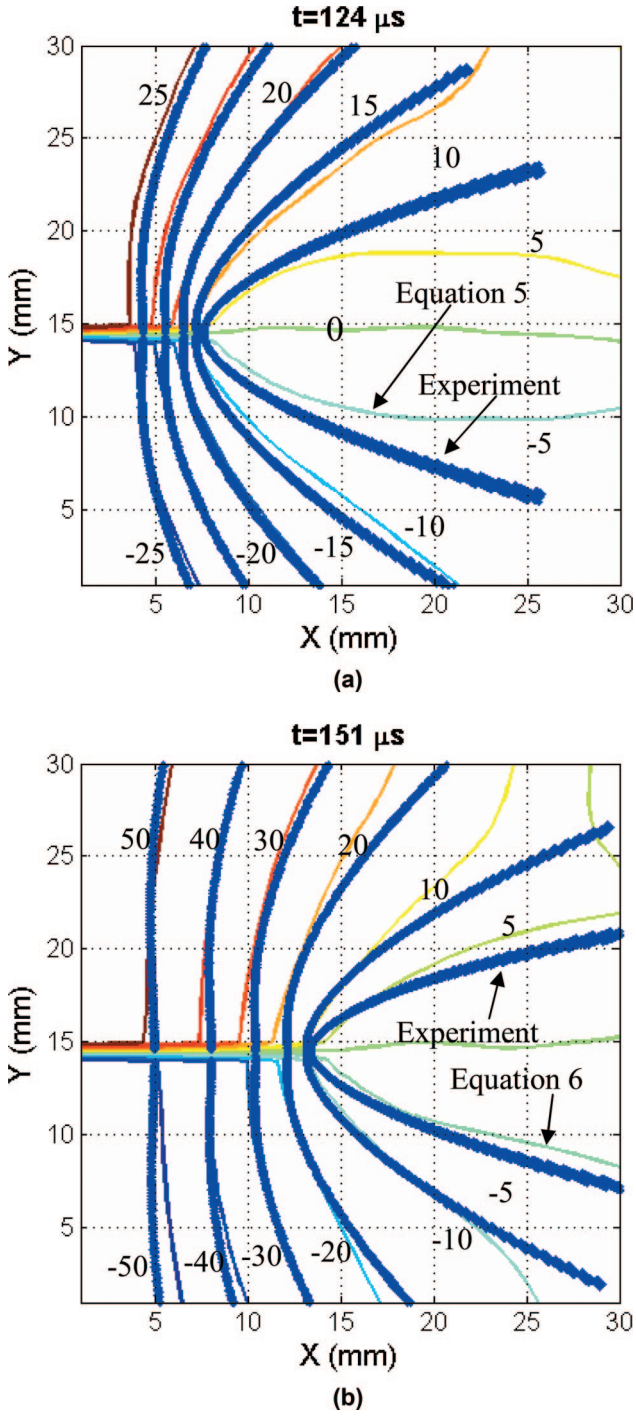

Fig. 12. (Color online) Examples showing quality of least-squares fit of displacement data; crack opening displacement field (μm) obtained from DIC and synthetic contours for (a) $t = 124$ μs (before crack initiation) and (b) $t = 151$ μs (after crack initiation); crack initiation time = 133 μs.

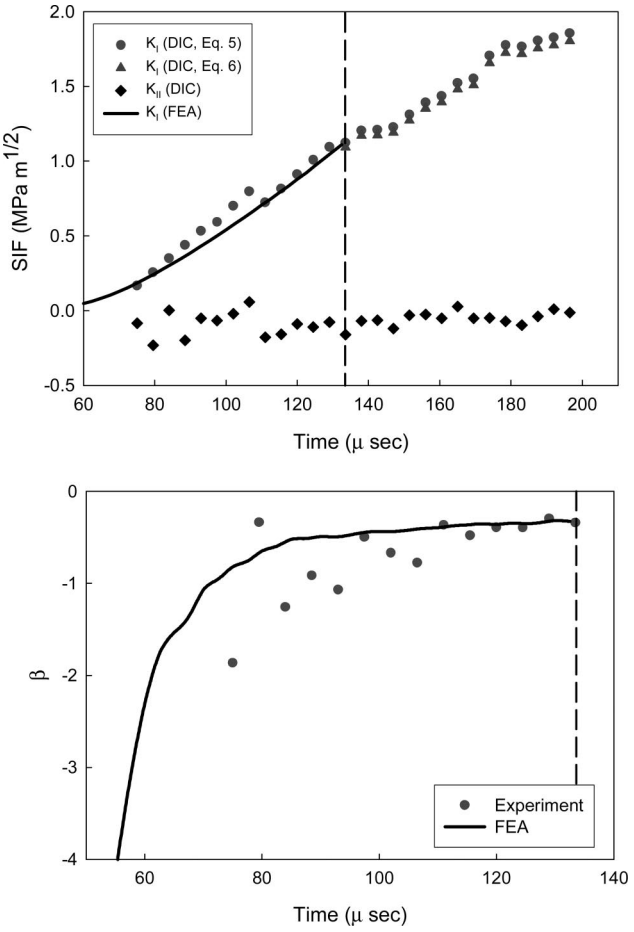

Fig. 13. (a) Stress intensity factors extracted from displacement field obtained from image correlation; SIF history obtained from finite element simulation up to crack initiation is also shown; (b) crack tip in-plane constraint; β obtained from experiments and finite element simulation. Broken line corresponds to crack initiation time.

were not available for analysis. The Mode II stress intensity factor, K_{II} remains close to zero within an acceptable experimental error, which is expected for a mode-I (symmetric loading relative to the crack) experiment reported here. This oscillation of K_{II} about zero represents errors associated with the evaluation of stress intensity factors using the least-squares method as well as loading asymmetries of the sample. The K_I history is in good agreement with the one from the finite element computation up to crack initiation. Once K_I and T-stress histories were extracted, the so-called planar crack tip constraint $\beta = T\sqrt{\pi a}/K_I$ was also computed and is plotted in Fig. 13(b) along with the one from the numerical simulation. A large negative β can be observed at the initial stages, which is typical of three-point bend geometries samples under dynamic loading conditions [38]. Just before crack initiation, the value of β is about −0.35, which is in agreement with authors from previous work [34]. A reasonably good agreement of experimental β with the computational values can also be seen from this figure.

7. Conclusion

The DIC technique combined with a rotating mirror-type high-speed digital camera is successfully developed for transient crack growth studies. A three-step approach is advanced for estimating displacements from decorated speckle images. The necessary steps to perform camera calibration and correct misalignments in the optical channels of the high-speed camera system are outlined. A set of benchmark experiments are conducted for the newly introduced camera system to assess the accuracy of displacements. In the present work, the displacements were resolved to an accuracy of 2% to 6% of a pixel (0.6 to 1.8 μm).

Using the developed methodology, dynamic crack growth behavior of a polymeric beam that was subjected to impact loading was studied. The entire crack tip deformation history from the time of impact up to complete fracture of the specimen was mapped. Time histories of failure characterization parameters, namely stress intensity factor and T stress are evaluated from the measured displacements. The measurements were in very good agreement with the companion finite element results. The current approach seems to be a powerful method to investigate dynamic failure events in real time. In a forthcoming paper, issues related to the measurement of strains, using the methodology and its feasibility for transient failure characterization of materials, will be examined.

The authors to thank the U.S. Army Research Office (Program Manager, Dr. Bruce LaMattina) for supporting this research through grants W911NF-04-10257 and DAAD19-02-1-0126 (DURIP).

References

1. J. G. A. de Graaf, "Investigation of brittle fracture in steel by means of ultra high speed photography," Appl. Opt. **3**(11), 1223–1229 (1964).
2. J. W. Dally, "Dynamic photo-elastic studies of fracture," Exp. Mech. **19**(10), 349–361 (1979).
3. V. Parameswaran and A. Shukla, "Dynamic fracture of a functionally gradient material having discrete property variation," J. Mater. Sci. **33,** 3303–3311 (1998).
4. H. V. Tippur, "Coherent gradient gensing: a Fourier optics analysis and applications to fracture," Appl. Opt. **31**(22), 4429–4439 (1992).
5. H. V. Tippur, S. Krishnaswamy, and A. J. Rosakis, "A coherent gradient sensor for crack tip measurements: Analysis and experimental results," Int. J. Fract. **48,** 193–204 (1991).
6. M. S. Kirugulige, R. Kitey, and H. V. Tippur, "Dynamic fracture behavior of model sandwich structures with functionally graded core; a feasibility study," Compos. Sci. Technol. **65,** 1052–1068 (2004).
7. M. S. Kirugulige and H. V. Tippur, "Mixed mode dynamic crack growth in functionally graded glass filled epoxy," Exp. Mech. **46,** 269–281 (2006).
8. Z. K. Guo and A. S. Kobayashi, "Dynamic mixed mode fracture of concrete," Int. J. Solids Struct. **32**(17), 2591–2607 (1995).
9. E. B. Flynn, L. C. Bassman, T. P. Smith, Z. Lalji, L. H. Fullerton, T. C. Leung, S. R. Greefield, and A. C. Koskelo, "Three-wavelength ESPI with the Fourier transform method for simulataneous measurement of microstructure scale deformations in three dimensions," Appl. Opt. **45**(14), 3218–3225 (2006).

10. T. Fricke-Begemann, "Three dimensional deformation field measurement with digital speckle correlation," Appl. Opt. **42**(34), 6783–6795 (2003).
11. R. Feiel and P. Wilksch, "High resolution laser speckle correlation for displacement and strain measurement," Appl. Opt. **39**(1), 54–60 (2000).
12. A. J. Moore, D. P. Hand, J. S. Barton, and J. D. C. Jones, "Transient deformation measurement with electronic speckle pattern interferometry and a high speed camera," Appl. Opt. **38**(7), 1159–1162 (1999).
13. G. Pedrini and H. J. Tiziani, "Double pulse electronic speckle interferometry for vibration analysis," Appl. Opt. **33**(34), 7857–7863 (1994).
14. D. E. Duffy, "Moiré gauging of in-plane displacement using double aperture imaging," Appl. Opt. **11**(8), 1778–1781 (1972).
15. R. S. Sirohi, J. Burke, H. Helmers, and K. D. Hinsch, "Spatial phase shifting or pure in-plane displacement and displacement-derivative measurements in ESPI," Appl. Opt. **36**(23), 5787–5791 (1997).
16. Y. J. Chao, P. F. Luo, and J. F. Kalthoff, "An experimental study of the deformation fields around a propagating crack tip," Exp. Mech. **38**(2), 79–85 (1998).
17. *Proceedings of the 2006 SEM Annual Conference and Exposition on Experimental and Applied Mechanics,* CD-ROM, June 4–7, 2006 (Saint Louis, Missouri).
18. *Proceedings of the International Society for Optical Engineering,* CD-ROM, Vols. 5580 and 6302.
19. D. Zhang, C. D. Eggleton, and D. D. Arola, "Evaluating the mechanical behavior of arterial tissue using digital image correlation," Exp. Mech. **42**(4), 409–416 (2002).
20. C. C. B. Wang, J. M. Deng, G. A. Ateshian, and C. T. Hung, "An automated approach for direct measurement of two-dimensional strain distributions within articular cartilage under unconfined compression," J. Biomed. Eng. **24,** 557–567 (2002).
21. E. B. Li, A. K. Tieu, and W. Y. D. Yuen, "Application of digital image correlation technique to dynamic measurement of the velocity filed in the deformation zone in cold rolling," Opt. Lasers Eng. **39,** 479–488 (2003).
22. J. N. Perie, S. Calloch, C. Cluszel, and F. Hild, "Analysis of multiaxial test on a C/C composite by using digital image correlation and a damage model," Exp. Mech. **42**(3), 318–328 (2002).
23. W. H. Peters and W. F. Ranson, "Digital image techniques in experimental stress analysis," Opt. Eng. (Bellingham) **21,** 427–431 (1982).
24. M. A. Sutton, W. J. Wolters, W. H. Peters, W. F. Ranson, and S. R. McNeil, "Determination of displacements using an improved digital image correlation method," Image Vis. Comput. **1**(3), 133–139 (1983).
25. H. A. Bruck, S. R. McNeill, M. A. Sutton, and W. H. Peters, "Digital image correlation using Newton-Raphson method of partial differential correction," Exp. Mech. **29,** 261–267 (1989).
26. D. J. Chen, F. P. Chiang, Y. S. Tan, and H. S. Don, "Digital speckle-displacement measurement using a complex spectrum method," Appl. Opt. **32**(11), 1939–1849 (1993).
27. P. F. Lou, Y. J. Chao, M. A. Sutton, and W. H. Peters, "Accurate measurement of three-dimensional deoformations in deformable and rigid bodies using computer vision," Exp. Mech. **33**(3), 123–132 (1993).
28. MATLAB 7.0, The MathWorks, Incorporated, http://www.mathworks.com, 2006.
29. C. G. Broyden, "The convergence of a class of double-rank minimization algorithms," J. Inst. Math. Appl., 76–90 (1970).
30. C. H. Reinsch, "Smoothing by spline functions," Numer. Math. **10,** 177–183 (1967).
31. P. Craven and G. Wahba, "Smoothing noisy data with spline functions: Estimating the correct degree of smoothing by the method of generalized cross validation," Numer. Math. **31,** 377–405 (1979).
32. R. C. Gonzalez, R. E. Woods, and S. L. Eddins, Digital image processing using MATLAB (Prentice Hall, 2004), 1st edition.
33. R. J. Butcher, C.-E. Rousseau, and H. V. Tippur, "A functionally graded particulate composite: Preparation, measurements and failure analysis," Acta Mater. **47**(1), 259–268 (1998).
34. M. J. Maleski, M. S. Kirugulige, and H. V. Tippur, "A method for measuring mode-I crack tip constraint under static and dynamic loading conditions," Exp. Mech. **44**(5), 522–532 (2004).
35. H. M. Westergaard, "Bearing pressure and cracks," J. Appl. Mech. **6,** A49–A53 (1939).
36. T. Nishioka and S. N. Atluri, "Path independent integrals, energy release rates, and general solutions of near-tip fields in mixed-mode dynamic fracture mechanics," Eng. Fract. Mech. **18**(1), 1–22 (1983).
37. J. W. Dally and W. F. Riley, *Experimental Stress Analysis,* 4th ed., College House Enterprises, LLC (2005).
38. K. Jayadevan, R. Narasimhan, T. Ramamurthy, and B. Dattaguru, "A numerical study in dynamically loaded fracture specimens," Int. J. Solids Struct. **38**(5), 4987–5005 (2001).